Evolution of low-altitude and ring current ENA emissions from a moderate magnetospheric storm: Continuous and simultaneous TWINS observations

P. Valek,[1,2] P. C. Brandt,[3] N. Buzulukova,[4] M.-C. Fok,[4] J. Goldstein,[1,2] D. J. McComas,[1,2] J. D. Perez,[5] E. Roelof,[3] and R. Skoug[6]

[1]   The moderate storm of 22 July 2009 is the largest measured during the extended solar minimum between December 2006 and March 2010. We present observations of this storm made by the two wide-angle imaging neutral-atom spectrometers (TWINS) mission. The TWINS mission measures energetic neutral atoms (ENAs) using sensors mounted on two separate spacecrafts. Because the two spacecrafts' orbital planes are significantly offset, the pair provides a nearly optimal combination of continuous magnetospheric observations from at least one of the TWINS platforms with several hours of simultaneous, dual-platform viewing over each orbit. The ENA imaging study presented in this paper is the first reported magnetospheric storm for which both continuous coverage and stereoscopic imaging were available. Two populations of ENAs are observed during this storm. The first are emissions from the ring current and come from a parent population of trapped ions in the inner magnetosphere. The second, low-altitude emissions (LAEs), are the result of precipitating ions which undergo multiple charge exchange and stripping collisions with the oxygen exosphere. The temporal evolution of this storm shows that the LAEs begin earlier and are the brightest emissions seen during the main phase, while later, during the recovery, the LAE is only as bright as the bulk ring current emissions.

Citation: Valek, P., P. C. Brandt, N. Buzulukova, M.-C. Fok, J. Goldstein, D. J. McComas, J. D. Perez, E. Roelof, and R. Skoug (2010), Evolution of low-altitude and ring current ENA emissions from a moderate magnetospheric storm: Continuous and simultaneous TWINS observations, *J. Geophys. Res.*, *115*, A11209, doi:10.1029/2010JA015429.

1. Introduction

[2]   Energetic neutral atoms (ENAs) are produced when local magnetospheric energetic ion populations undergo charge exchange with cold geocoronal neutral hydrogen or with exospheric oxygen atoms at low altitudes. ENA imaging of the terrestrial magnetosphere dates back to serendipitous observations from the MEPI instrument, flown on ISEE 1 [*Williams et al.*, 1978] and designed to measure not ENAs but energetic particles [*Roelof*, 1987]. Since then, various groups have developed instruments specifically targeting ENA observations with progressively higher sensitivity and better angular resolution and have extended the energy range [*McComas et al.*, 1991, 1998a]. In March 2000, the IMAGE

spacecraft [*Burch*, 2000] was launched into a high-altitude, high-inclination polar orbit carrying three ENA imaging instruments: HENA covering ~20–500 keV [*Mitchell et al.*, 2000], MENA covering ~1–30 keV [*Pollock et al.*, 2000], and LENA covering ~10–300 eV [*Moore et al.*, 2000].

[3]   ENA observations from IMAGE have been analyzed in numerous and diverse scientific studies, which have broadened and extended the understanding of our dynamic magnetosphere, including substantial contributions to the understanding of magnetospheric substorms [*Pollock et al.*, 2003, and references therein; *Huang et al.*, 2003] and storms [*Brandt et al.*, 2001; *Pollock et al.*, 2001; *McComas et al.*, 2002; *Skoug et al.*, 2003; *Perez et al.*, 2004a, 2004b; *Reeves et al.*, 2003; *DeMajistre et al.*, 2004; *Roelof et al.*, 2004; *Roelof*, 2005; *Vallat et al.*, 2004; *Henderson et al.*, 2006; *Zaniewski et al.*, 2006; *Denton et al.*, 2005, 2007].

[4]   As valuable as the IMAGE ENA observations were, they suffered from two fundamental limitations that affect any single Earth-orbiting spacecraft: 1) the instruments had to be turned off during perigee passes, creating ~4 h gaps during each ~14 h orbit, and 2) imaging could be made from only a single location, making it very difficult to resolve three-dimensional structure in magnetospheric plasmas. In contrast, the two wide-angle imaging neutral-atom spectrometers

---

[1]Southwest Research Institute, San Antonio, Texas, USA.
[2]Also at Department of Physics, University of Texas, San Antonio, Texas, USA.
[3]Johns Hopkins University Applied Physics Laboratory, Laurel, Maryland, USA.
[4]NASA Goddard Space Flight Center, Greenbelt, Maryland, USA.
[5]Department of Physics, Auburn University, Auburn, Alabama, USA.
[6]Los Alamos Laboratory, Los Alamos, New Mexico, USA.

(TWINS) mission [*McComas et al.*, 2009a] was designed to image the magnetosphere simultaneously from two independent high-altitude, high-inclination platforms. The two spacecrafts are in Molniya orbits (63.4° inclination and 12 h orbital period) with 10^3 km perigee altitudes and apogees in the Northern Hemisphere at ~7.2 R_E. The spacecraft are three-axis stabilized and provide approximately nadir pointing of the TWINS instruments. Because the two spacecrafts' orbital planes are significantly offset, the pair provides a nearly optimal combination of continuous magnetospheric observations from at least one of the TWINS platforms with several hours of simultaneous, dual-platform viewing over each orbit. The ENA imaging study presented in this paper is the first reported magnetospheric storm for which both continuous coverage and stereoscopic imaging were available.

[5] The Sun was in a remarkably prolonged solar minimum (beginning of solar cycle 24) that had only small to moderate storms. The moderate storm of 22 July 2009 produced a peak *Dst* of −79 nT, which is the largest measured between December 2006 and March 2010. In the year previous to the 22 July 2009 storm, there were only 15 events when *Dst* fell below −30 nT, and only 2 occurrences when *Dst* went below −50 nT. During the previous solar minimum, from July 1996 to July 1997 there were more than 30 times when *Dst* dropped below −30 nT, and 3 storms when *Dst* went below −100 nT (*Dst* data from Kyoto data service). In this study, we present the TWINS observations of the 22 July 2009 moderate storm.

2. Instrumentation

[6] The TWINS imagers are based upon the slit camera concept [*McComas et al.*, 1998a] originally flown on the MENA instrument [*Pollock et al.*, 2000]. This design provides a very large aperture, and hence the geometric factor, required to properly image ENAs across the critical energy range from ~1 keV to many tens of kiloelectron volts. For TWINS, two sensors heads are used to acquire an instantaneous 1-D spatial image and full energy spectrum of the ENAs. A full image is acquired by mounting the sensor heads on a rotating actuator, which sweeps back and forth over an approximately Earth-centered viewing cone. Neutral atoms are detected and recorded at very high angular resolution (~1°) with $\Delta E/E$ ~1.0 for H atoms. Full images are taken in 60 s typically every 72 s. Furthermore, compared to MENA, with an energy range of ~1–30 keV/amu, TWINS observations have been extended to cover the widely used low-energy end of the IMAGE/HENA and measure ENAs from <1 keV/amu up to ~100 keV/amu.

[7] The TWINS instrument uses ultrathin carbon foils mounted at the aperture to make a coincidence time of flight (TOF) measurement. Ultrathin carbon foils (~50 Å thick), mounted on highly transmissive grids, have been used successfully in a wide variety of space missions [*McComas et al.*, 2004]. The forward secondary electron yield of H$^+$ transiting thin carbon foils has been measured to range from 2.1 to 4.5 over an energy range of 10–90 keV, with larger yields for heavier ions with the same energy per amu [*Ritzau and Baragiola*, 1998]. Because hydrogen reaches charge-state equilibrium before it exits the foil, the forward secondary electron yield for H should equal that of H$^+$. The foil is biased to −2 kV so that secondary electrons are accelerated toward a 70 line-per-inch grounded acceleration grid. Therefore, secondary electrons are quickly accelerated toward the "start" anode region of the microchannel plate (MCP) detector. This acceleration enables the detected position of the secondary electrons on the detector to accurately represent the locations at which ENAs transited the foil. The ENA trajectory measurements are obtained using the detected positions of an ENA and its associated secondary electrons. The TOF measurement is derived from the time difference between detection of the secondary electrons, which are detected first, and the ENA.

[8] A perturbation that results from using start foils for timing is that the incident particles undergo energy straggling and angle scattering as they pass though the foils. The magnitudes of these effects are functions of (1) the foil properties, (2) the foil thickness, and (3) the incident energy and species of the particle passing though the foil [*Funsten et al.*, 1993; *Allegrini et al.*, 2006]. For particles arriving at the carbon foils with the same incident angle and energy, more massive particles experience larger energy loss and angular scattering. Because of this, the TWINS instrument will make higher-resolution measurements of the hydrogen ENAs than of the oxygen ENAs. The magnitude of the energy straggling and angular scattering is reduced for all species as the foil thickness is reduced. To minimize the energy straggling and angular scattering, carbon foils as thin as those reliably flown to date are used in TWINS (nominal thickness ~0.5 $\mu g/cm^2$) [*McComas et al.*, 2004].

[9] Since TWINS actively images in only one spatial dimension, angular scattering effects are limited to that dimension. Intense ENA emissions can scatter and create artifacts that appear as extended emissions in the imaging direction. Lower-energy and more massive ENAs will produce the largest scattering artifacts. Low-energy oxygen ENAs will scatter across a wide angular range even if they are coming from a localized region in space. The angular scattering effects occur in the radial direction of the TWINS images shown in Figures 1 and 2 and are of the order of 4° full width at half maximum (FWHM) for 8 keV hydrogen.

[10] The differences in the carbon foil electron yields for incident H and O can be used to determine the mass of the ENAs measured by TWINS. The pulse height distribution exiting the MCP detector in the start region will be larger for larger electron yields. This technique has been used successfully on the magnetosphere imaging instrument (MIMI) [*Krimigis et al.*, 2004] and HENA [*Mitchell et al.*, 2003] ENA imagers. For the TWINS energy range, the pulse height distributions for H and O have significant overlap. This requires a relatively large number of ENAs to be collected to determine the relative fraction of H and O ENAs. The required accumulation times are of the order of hours, especially in regions where the flux is typically low (~>2 R_E). Since we are investigating the temporal evolution of this storm, we have included only the total flux of ENAs as a function of energy per amu.

[11] In addition, the Ly-α imagers on TWINS allow continuous monitoring of the geocorona, independently measuring the cold charge-exchange neutrals that produce the observed ENAs. Finally, environmental sensors on the TWINS spacecraft make simultaneous measurements of the local charged particle environment. See the work of
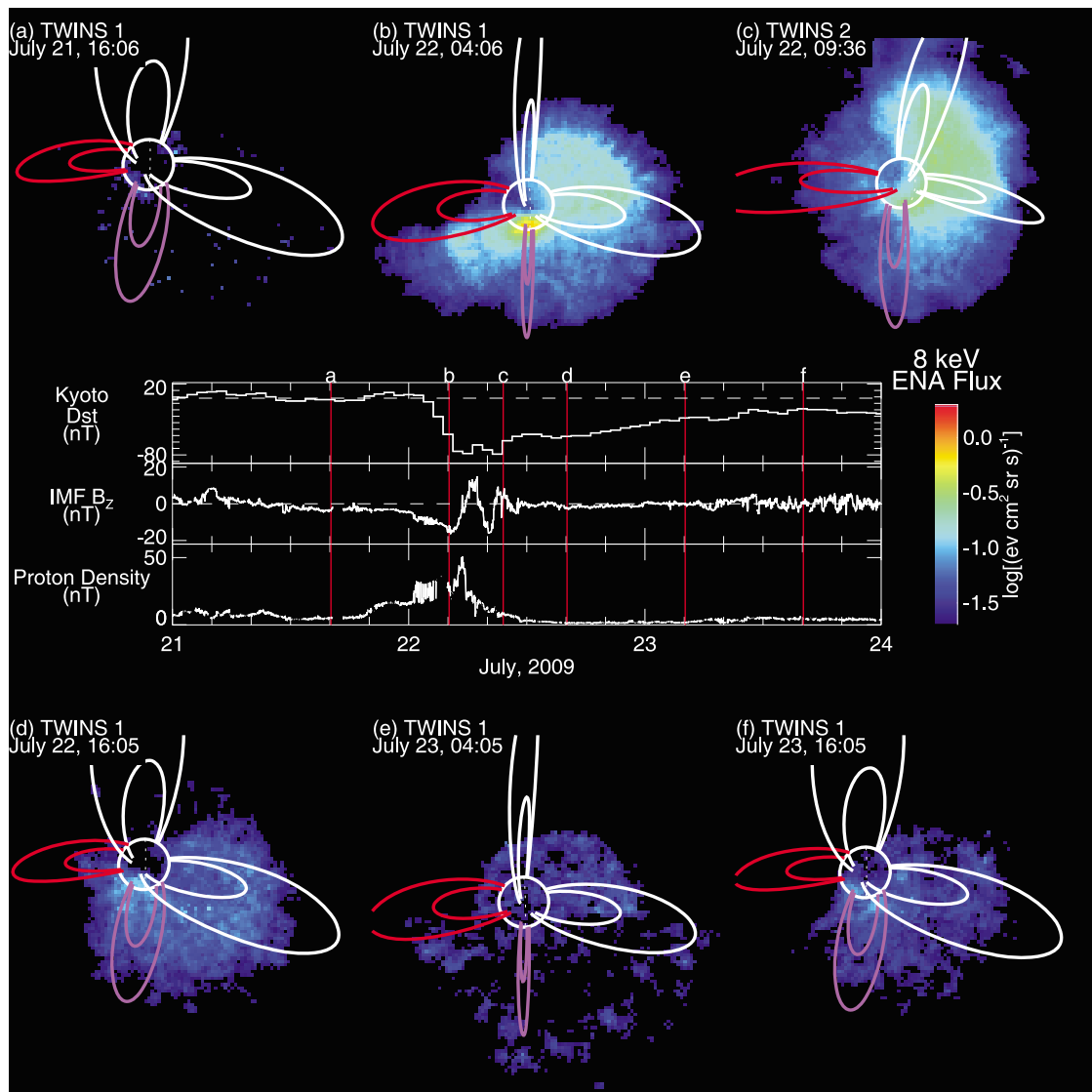
Figure 1. The moderate storm of 22 July 2009. Middle panels show *Dst*, interplanetary magnetic field (IMF) Bz, and solar wind density from 21 through 24 July. Solar wind parameters are from ACE and have been time shifted to the location of the bow shock. The images along the top and bottom of this figure are all of 8 keV/amu energetic neutral atoms (ENAs) as seen by either TWINS 1 or TWINS 2. Color bar to the right of the *Dst* and solar wind plots is common to all TWINS images shown in this paper. Vertical red lines through the line plots are at the times of the TWINS images. Each TWINS image is taken at apogee. Limb of the Earth and dipole field lines for *L* = 4 and 8 are drawn to aid viewing. Red field lines are in the sunward direction; purple lines are in the duskward direction.

McComas et al. [2009a] for addition information on TWINS, its Ly-α imagers, and the environmental monitors.

3.   Observations

[12]   The ENA images in this study use a fisheye projection, as shown in Figures 1a–1f. The total field of view (FOV) extends to 60° from the center of the image. The limb of the Earth and dipole magnetic field lines for *L* = 4 and 8 are drawn as guides; noon (1200 MLT) and dusk (1800 MLT) field lines are colored red and purple, respectively. The TWINS instruments were in the Northern Hemisphere for all these images. TWINS is approximately a nadir-viewing instru-

ment, but the center of the images is offset from the center of the Earth by approximately 10°. The same logarithmically scaled color bar is employed for all images in this paper. All ENA images shown here are in an 8 ± 4 keV/amu band; that is, the energy band is an integration of ENAs in the range 4–12 keV/amu.

[13]   The TWINS images shown here were processed to have a statistically significant number of counts in each pixel. If the counts in a given pixel are less than a specified target value, counts from the surrounding nearest neighbors are added until the target value is reached. When this value is reached, the new counts total and commensurate geometric factor are then recorded for that pixel in a new array. The

counts and geometric factor over the region of contributing pixels are combined to calculate the correct intensity. In regions of the image with high counts, only a small area is needed to reach the target value, while in regions of low counts, the areas become larger. Thus, this dynamic method requires the least amount of smoothing needed to achieve any particular statistical certainty. This dynamic smoothing method was first used with the ENA imaging of the heliosphere by the Interstellar Boundary Explorer mission [*McComas et al.*, 2009b]. The minimum number of counts is determined for the entire image and sets the maximum error due to counting statistics. For the images here, the target value was chosen such that there will be a spatial resolution of $5° \times 5°$ on average across the image. The target value in each image is the average number of counts per pixel divided by 25 pixels. The images taken with low incident ENA flux (prior to the storm and late in the recovery phase; Figures 1a, 1e, and 1f) will have the largest uncertainties owing to counting errors. The images taken during the storm main phase and early recovery all have errors from counting statistics that are less than 25%.

[14] For each of these images, a simple background subtraction was performed. The average, measured flux in the annulus 2° wide at the outer edge of the images is subtracted from the whole image. Any negative values that result from this difference are set to 0. The average flux at the edge of the image should be negligible. For times when there is a penetrating background, the background is elevated uniformly across the whole image.

[15] Figure 1 (middle) shows the real-time *Dst* as provided by Kyoto, the interplanetary magnetic field (IMF) Bz, and the solar wind proton density. The IMF Bz [*Smith et al.*, 1998] and solar wind proton density [*McComas et al.*, 1998b] data are from the advanced composition explorer (ACE) spacecraft [*Stone et al.*, 1998] and have been time shifted to the location of the bow shock by OmniWeb. The vertical red bars indicate the times of the ENA images shown above and below these panels. For the week prior to the storm, the total IMF was low (2–4 nT). The proton density was also low (5–10 cm^{-3}), and the solar wind speed was below 300 km/s before the storm onset. On 22 July, the IMF turned strongly southward, and the proton density increased to a peak value of ~50 cm^{-3}. The proton speed (not shown) increased steadily from ~300 km/s before 22 July to speeds of ~500 km/s on 23 July.

[16] Returning to the six ENA images in Figure 1, 1a is an image prior to the storm. The magnetosphere was in a very quiet state, and very low ENA fluxes were observed. This image shows the typical minimum ENA fluxes seen by TWINS. Figure 1b shows an image of the ENAs near the peak of the storm. This image is dramatically brighter than the prestorm conditions. The brightest emissions seen in this image are low-altitude emissions (LAEs). The LAE is due to precipitating ions charge exchanging at low altitudes (~500 km) [*Roelof*, 1997]. In this region, the geocorona is sufficiently dense that the optically thin approximation (a single charge exchange collision before observation) for charge exchange is not valid; instead, a thick target approximation is required [*Bazell et al.*, 2010]. A precipitating ion can undergo multiple charge exchange and stripping colli-

sions in which it becomes neutralized and then re-ionized before finally exiting as an ENA. The energy loss per collision is only 0.1%–1.0% of the incident energy in the 3–30 keV range, so the precipitating particle can change back and forth between charge states without losing a significant fraction of its energy or suffering a significant deflection from its path. Interestingly, the pitch angle information of the precipitating ion is largely retained during these multiple collisions.

[17] LAE ENAs exit with pitch angles near ~90° [*Pollock et al.*, 2009]. Owing to the inclination of the Molniya orbit, TWINS has a favorable viewing of LAEs at local times ~12 h away from the spacecraft location. This means that TWINS preferentially sees the LAEs in the duskward direction in Figure 1b. These observations should not be interpreted to suggest that the LAEs are constrained only to this narrow region of local time, but rather that the particular viewing geometry enables viewing of only specific LAEs [*Bazell et al.*, 2010].

[18] Also visible in Figure 1b are ring current emissions. They were observed at nearly all local times except for the morning sector. The brightest ring current emissions were in the post-midnight sector. The ring current emissions were not as bright as the LAE, but they were still dramatically brighter than in the prestorm image. A substorm was also seen at this time, with the AE index reaching ~1250 nT at 0400 UT. The extended enhancement in the image that runs from the dayside through the LAE to the nightside may be partly a result of scattering of the LAE in the carbon foils.

[19] Figure 1c shows the inner magnetosphere at the very beginning of the recovery phase. At this time, the intensity of the LAE was no longer brighter than that of the ring current. The ring current emissions were more intense than those observed earlier during the storm onset (Figure 1b). A substorm was also seen at this time, with the AE index reaching ~750 nT at 0900 UT. The ring current still had the brightest emissions in the postmidnight sector. However, the ring current emissions are seen at all local times, filling in the morning sector that was empty in Figure 1b.

[20] The inner magnetosphere after about 6 h of recovery is shown in Figure 1d. The ring current still had bright emissions but was weaker than seen earlier in the storm at either the peak (Figure 1b) or early recovery (Figure 1c). The emissions drifted westward to the early evening sector. During late recovery (Figures 1e and 1f), we see the ENA emissions returning to near prestorm levels.

[21] The relative intensity changes of the LAE and ring current emissions from Figure 1b to Figure 1c suggest that the LAE may have peaked before the ring current for this storm. To investigate the timing of the LAE and ring current evolution, ENA images were taken every 15 min throughout this storm. Selected images are shown across the bottom of Figure 2. The images in Figures 2a through 2d and Figure 2h were taken with TWINS 1, and those in Figures 2e through 2g were taken with TWINS 2. Figures 2a through 2d show the evolution of the magnetosphere during the main phase. Growth during a substorm is shown in Figures 2f and 2g, in which the ring current transitions from symmetric to asymmetric. Early recovery is shown in Figure 2h. The LAE are a localized phenomenon, so the viewing geometry can be
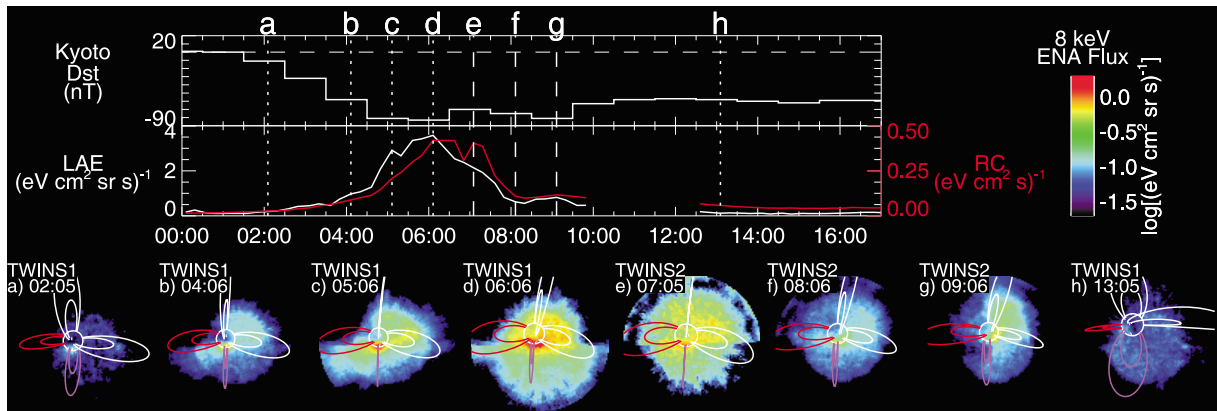
Figure 2. The evolution of the ENA emissions are shown from onset of the 22 July 2009 storm through early recovery. (top) Dst and the low-altitude emission (LAE) and ring current (RC) indices. LAE index (white curve) is the peak flux per pixel measured within $2R_E$. RC index (red curve) is the integral of flux over the TWINS FOV, not including the region inside of $2R_E$. (below) Vertical dotted (dashed) lines though Figure 2 (top) indicate the times of the TWINS 1 (TWINS 2) images. To aid in comparison, the same color bar is used for the images as in Figure 1.

important. Owing to the orbits of the TWINS spacecraft, TWINS 1 and TWINS 2 had common viewing geometries for this time. TWINS 1 at 0506 UT (Figure 2c) and TWINS 2 at 0705 UT (Figure 2e) both viewed the inner magnetosphere toward the duskward direction. Later, TWINS 1 looked toward early evening (Figure 2d), and TWINS2 had a similar viewing geometry (Figures 2f and 2g). The small change in viewing geometry between Figures 2f and 2g is not considered significant.

[22] We have found it useful to define two single indices that approximately characterize these complex but related phenomena. Since the LAE is a localized emission, the brightest pixel inside of $2 R_E$ is used as an index of the LAE intensity. The integral of the ENA flux outside of $2R_E$ is used as a ring current index and is referred to as RC here. The middle panel of Figure 2 plots the indices for the LAE (in white) and ring current (in red) for this storm in the same 8 keV/amu channel used for the ENA images. The top panel of Figure 2 has Dst plotted again for context. Vertical dotted (dashed) lines drawn across the Dst and LAE/RC plots show the times of the TWINS 1 (TWINS 2) images below. The label above each vertical line corresponds to the images below. There is a gap between ~1000 and 1230 UT. During this time period, high fluxes of ions were seen in the environmental monitors (T. Guild, personal communication) flown on the same spacecraft as TWINS [McComas et al., 2009a]. A fraction of the ions got past the ion-rejection collimators, resulting in an elevated background level. Because of this, we do not show the ENA data from this time period.

[23] Both the LAE and RC were at low levels from the start of this storm. From 0000 to 0330 UT, the LAE and RC had similar growth, with the LAE having the brightest signature throughout the main phase of the storm. Starting around 0400 UT, the LAE grew more rapidly than the RC. This was also the time when the IMF Bz started turning more northward. The IMF Bz became positive at ~0600 UT. The LAE signal rose quickly from ~0400 to 0500 UT, with the largest increase between 0430 and 0500 UT. The LAE continued to increase with a peak at 0600 UT. From 0600 to 0800 UT, the LAE dropped off slowly.

[24] The RC index showed a different timing than the LAE starting around 0400 UT. From 0400 to 0600 UT, the RC increased more slowly than the LAE. The RC index growth rate increased starting at ~0430 UT. The RC index reached its peak values around 0600 UT and then maintained this level for approximately an hour, after which it dropped rapidly during the next hour. Both the LAE and RC indices reach a local maximum around 0900 UT. This may be the result of a substorm at this time.

[25] Figure 3 shows the RC and LAE indices as a function of energy over the same time period as in Figure 2. The RC fluxes peaked at around 2 keV/amu. The lower-energy RC emissions tended to vary more smoothly over time than the higher-energy RC emissions. The LAE emissions are peaked more toward higher energies (8 keV/amu).

4. Discussion

[26] LAEs are produced by precipitation of RC ions into the upper atmosphere, where they undergo charge exchange multiple times and some fraction is re-emitted as neutrals. Thus, one might have assumed that the LAE and RC emissions would closely match each other in time. However, here we have found that the temporal evolutions of the LAE and ring current emission actually behave differently during this medium-sized storm. Here the LAE begins earlier and is the brightest emission seen during the main phase, while later, during the recovery, the LAE is only as bright as the bulk ring current emissions.

[27] In general, the intensity of ENAs reaching an instrument is an integral of the energy-dependent charge exchange cross section, the density of the neutral population, the ion intensity, and an attenuation factor. The attenuation factor accounts for the loss of ENAs between their emission point and the spacecraft and can involve multiple collisions. Either deconvolution [J. D. Perez et al., Validation of a method for obtaining ion intensities from ENA images using data from TWINS and THEMIS, submitted to *Journal of Geophysical Research*, 2010] or forward modeling [Brandt et al., 2001] is required to extract the parent ion distributions from the ENA
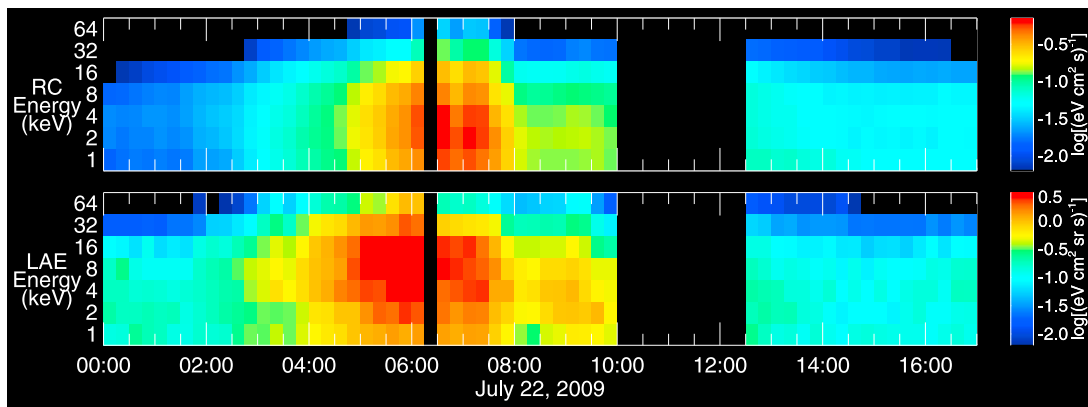
Figure 3. The LAE and RC indices are plotted as a function of energy and time. Each energy bin is centered on the energy indicated and has a width of 100% (i.e., the bin labeled 4 keV includes ENAs from 2 to 6 keV). Although faint, the LAE is seen starting at 0000 UT. LAE is most intense during the onset of the storm and fades to below the RC levels during the recovery phase. An energy dispersion can be seen in the LAE, with ENAs in the 4–8 keV range seen first and lower energies seen later. Unlike the LAE, the RC does not appear to have strong energy dispersion.

images of the ring current. In this region, the thin-target approximation of a single charge exchange collision with no attenuation of the ENAs is used. For the LAE, since a multicollision process is involved, a more detailed formulation of the ENA generation process is required. See the work of *Bazell et al.* [2010] for a more detailed description of the ENA generation process for LAEs. However, a quantity proportional to the energy spectra of the ion distributions can be obtained directly from the ENA images for both the optically thin and optically thick cases.

[28] For the ring current, the thin-target approximation can be used. This implies that the measured ENA has experienced a single charge exchange collision with no attenuation of the ENAs. In this case, the ENA flux is proportional to the ion flux and the hydrogen charge exchange cross section,

$$\langle J_{ion,RC} \rangle \propto \frac{1}{\sigma^{10}} \langle J_{ENA,RC} \rangle, \tag{1}$$

where $\langle J_{ion,RC} \rangle (E) = \int d\Omega J_{ion,RC}(E)/\Delta\Omega$ and $\langle J_{ENA,RC} \rangle (E) = \int d\Omega J_{ENA,RC}(E)/\Delta\Omega$. The charge exchange cross section is σ^{10}, and $J_{0,RC}$ ($J_{ENA,RC}$) is the parent ion population (ENA population) in the ring current integrated over an ENA pixel.

[29] A thick-target approximation (TTA) is required for the LAE. In this approximation, not only ENA production but also ENA attenuation must be considered. For the TTA, only stripping collisions are considered in the attenuation of the ENAs. A precipitating ion may change charge state multiple times, but the total energy change in the process is small compared to the incident energy for ENAs seen in the TWINS energy range. The TTA from *Bazell et al.* [2010] is

$$\langle J_{ion,LAE} \rangle \propto \left(1 + \frac{\sigma^{01}}{\sigma^{10}}\right) \langle J_{ENA,LAE} \rangle, \tag{2}$$

where $\langle J_{ion,LAE} \rangle (E) = \int d\Omega J_{ion,LAE}(E)/\Delta\Omega$ and $\langle J_{ENA,LAE} \rangle (E) = \int d\Omega J_{ENA,LAE}(E)/\Delta\Omega$; σ^{01} is the stripping cross section.

[30] Using the thin-target approximation (equation (1)) with the ring current ENAs and the thick target approximation (equation (2)) with the LAEs, the indices shown in Figure 3

can be transformed into quantities that show the energy spectrum of the parent ion populations. This is shown in Figure 4. Both the proportional RC energy spectrum and the LAE spectrum are normalized to the peak values seen in this time period.

[31] Thus, in addition to the different timing seen in the ENA images, Figure 4 shows that the parent populations of the LAE and ring current have different energy spectra. The LAE parent population is more peaked in energy during the times when substorms are seen (∼0400 and 0900 UT). The ring current parent population has a rather flat spectrum during this time but is more peaked during the early recovery.

[32] There are multiple possible reasons for the differences in energy spectra between the two indices. First, since the LAEs are produced by precipitating ions, the differences in the energy spectra may show the differences between particles inside and outside of the loss cone. Next, the LAE and RC indices are defined to include ENAs from different local times. A rule of thumb for the TWINS mission is that the LAEs are generally seen at local times 12 hours from the location of the spacecraft. For this study, the LAE index is determined using ENAs from local times near dusk. The RC index is determined using ENAs from all local times. The local time dependence of these indices cannot be discerned from this one storm. Finally, in this study we did not use mass-resolved ENA data. These effects will be investigated in future studies.

[33] Since the LAE is produced lower in the atmosphere, where the geocorona is far more dense, the LAE are generated more efficiently than ENA emissions directly from the ring current. Thus, the LAE can provide earlier indications of an enhancement in the RC ions population than direct ENA observations of the RC itself. This new feature may have implications for space weather applications of ENA imaging, where early detection and measurement could provide an edge in real-time space storm tracking.

[34] The dimmer LAE observed later in the storm is probably an indication of emptying of the loss cone. If so, TWINS observations also provide a new opportunity to
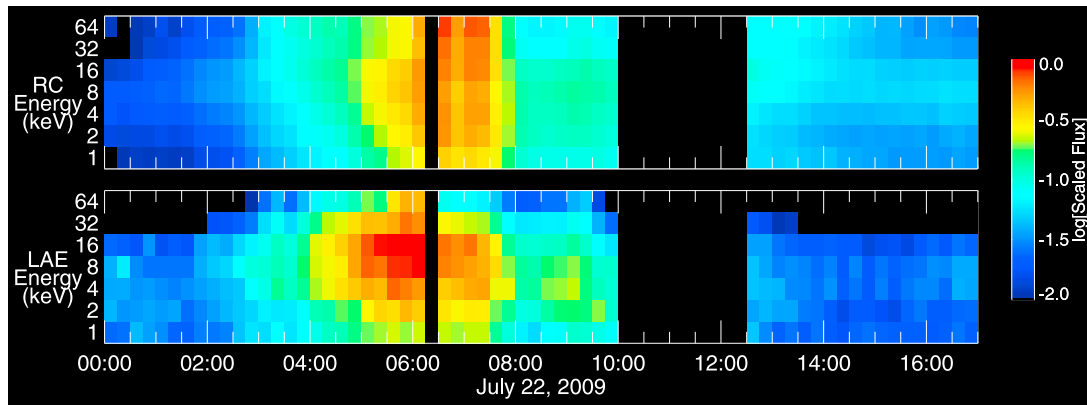
Figure 4. The RC and LAE indices shown in Figure 3 are scaled to be proportional to the parent ion population. RC ion spectrum is determined using an optically thin approximation, and the LAE ion spectrum is determined using an optically thick approximation. Since both the LAE and RC spectra are proportional to the parent ion populations, they have both been normalized to the peak value seen during this time period.

directly measure the rate at which the loss cone empties and assess the balance between this emptying and the diffusion rate of particles into the loss cone.

[36] Masaki Fujimoto thanks the reviewers for their assistance in evaluating this manuscript.

References

Allegrini, F., D. J. McComas, D. T. Young, J.-J. Berthelier, J. Covinhes, J.-M. Illiano, J.-F. Riou, H. O. Funsten, and R. W. Harper (2006), Energy loss of 1–50 keV H, He, C, N, O, Ne, and Ar ions transmitted through thin carbon foils, *Rev. Sci. Instrum.*, 77(4), doi:044501.1-044501.7.

Bazell, D., E. C. Roelof, T. Sotirelis, P. C. Brandt, H. Nair, P. Valek, J. Goldstein, and D. McComas (2010), Comparison of TWINS images of low-altitude emission of energetic neutral atoms with DMSP precipitating ion fluxes, *J. Geophys. Res.*, 115, A10204, doi:10.1029/2010JA015644.

Brandt, P. C., S. Barabash, E. C. Roelof, and C. J. Chase (2001), Energetic neutral atom imaging at low altitudes from the Swedish microsatellite Astrid: Extraction of the equatorial ion distribution, *J. Geophys. Res.*, 106(A11), 25,731–25,744.

Burch, J. L. (2000), IMAGE mission overview, *Space Sci. Rev.*, 91(1–2), 1–14.

DeMajistre, R., E. C. Roelof, P. C. Brandt, and D. G. Mitchell (2004), Retrieval of global magnetospheric ion distributions from high-energy neutral atom (ENA) measurements by the IMAGE/HENA instrument, *J. Geophys. Res.*, 109, A04214, doi:10.1029/2003JA010322.

Denton, M. H., V. K. Jordanova, M. G. Henderson, R. M. Skoug, M. F. Thomsen, C. J. Pollock, S. Zaharia, and H. O. Funsten (2005), Storm-time plasma signatures observed by IMAGE/MENA and comparison with a global physics-based model, *Geophys. Res. Lett.*, 32, L17102, doi:10.1029/2005GL023353.

Denton, M. H., M. F. Thomsen, B. Lavraud, M. G. Henderson, R. M. Skoug, H. O. Funsten, J. M. Jahn, C. J. Pollock, and J. M. Weygand (2007), Transport of plasma sheet material to the inner magnetosphere, *Geophys. Res. Lett.*, 34, L04105, doi:10.1029/2006GL027886.

Funsten, H. O., D. J. McComas, and B. L. Barraclough (1993), Ultrathin foils used for low-energy neutral atom imaging of the terrestrial magnetosphere, *Opt. Eng.*, 31, 3090–3095.

Henderson, M. G., G. D. Reeves, R. Skoug, M. F. Thomsen, M. H. Denton, S. B. Mende, T. J. Immel, P. C:son Brandt, and H. J. Singer (2006), Mag-

netospheric and auroral activity during the 18 April 2002 sawtooth event, *J. Geophys. Res.*, 111, A01S90, doi:10.1029/2005JA011111.

Huang, C.-S., J. C. Foster, G. D. Reeves, G. Le, H. U. Frey, C. J. Pollock, and J.-M. Jahn (2003), Periodic magnetospheric substorms: Multiple space-based and ground-based instrumental observations, *J. Geophys. Res.*, 108(A11), 1411, doi:10.1029/2003JA009992.

Krimigis, S. M., et al. (2004), Magnetosphere Imaging Instrument (MIMI) on the Cassini mission to Saturn/Titan, *Space Sci. Rev.*, 114, 233–329.

McComas, D. J., B. L. Barraclough, R. C. Elphic, H. O. Funsten III, and M. F. Thomsen (1991), Magnetospheric imaging with low-energy neutral atoms, *Proc. Natl. Acad. Sci.U. S. A.*, 88, 9598–9602.

McComas, D. J., H. O. Funsten, and E. E. Scime (1998a), Advances in low-energy neutral atom imaging, in *Measurement Techniques in Space Plasmas: Fields*, Geophys. Monogr. Ser., vol. 103, edited by R. F. Pfaff, J. E. Borovsky, and D. T. Young, pp. 275–280, AGU, Washington, D. C.

McComas, D. J., S. J. Bame, P. Barker, W. C. Feldman, J. L. Phillips, P. Riley, and J. W. Griffee (1998b), Solar Wind Electron Proton Alpha Monitor (SWEPAM) for the Advanced Composition Explorer, *Space Sci. Rev.*, 86, 563–612.

McComas, D. J., P. Valek, J. L. Burch, C. J. Pollock, R. M. Skoug, and M. F. Thomsen (2002), Filling and emptying of the plasma sheet: Remote observations with 1–70 keV energetic neutral atoms, *Geophys. Res. Lett.*, 29(22), 2079, doi:10.1029/2002GL016153.

McComas, D. J., F. Allegrini, C. J. Pollock, H. O. Funsten, S. Ritzau, and G. Gloeckler (2004), Ultrathin (~10 nm) carbon foils in space instrumentation, *Rev. Sci. Instrum.*, 75(11), 4863–4870, doi:10.1063/1.1809265.

McComas, D. J., et al. (2009a), The Two Wide-Angle Imaging Neutral-Atom Spectrometers (TWINS) NASA Mission-of-Opportunity, *Space Sci. Rev.*, 142, 157–231, doi:10.1007/s11214-008-9467-4.

McComas, D. J., et al. (2009b), Global observations of the interstellar interaction from the Interstellar Boundary Explorer (IBEX), *Science*, 326, 959–962, doi:10.1126/science.1180906.

Mitchell, D. G., et al. (2000), High-Energy Neutral Atom (HENA) imager for the IMAGE mission, *Space Sci. Rev.*, 91, 67–112.

Mitchell, D. G., P. C. Brandt, E. C. Roelof, D. C. Hamilton, K. C. Retterer, and S. Mende (2003), Global imaging of O+ from IMAGE/HENA, *Space Sci. Rev.*, 109, 63–75.

Moore, T. E., et al. (2000), The low-energy neutral atom imager for IMAGE, *Space Sci. Rev.*, 91, 155–195.

Perez, J. D., X.-X. Zhang, P. C. Brandt, D. G. Mitchell, and C. J. Pollock (2004a), Dynamics of ring current ions as obtained from IMAGE HENA and MENA ENA images, *J. Geophys. Res.*, 109, A05208, doi:10.1029/2003JA010164.

Perez, J. D., X.-X. Zhang, P. C. Brandt, D. G. Mitchell, J.-M. Jahn, C. J. Pollock, and S. B. Mende (2004b), Trapped and precipitating protons in the inner magnetosphere as seen by IMAGE, *J. Geophys. Res.*, 109, A09202, doi:10.1029/2004JA010421.

Pollock, C. J., et al. (2000), Medium-Energy Neutral Atom (MENA) imager for the IMAGE mission, *Space Sci. Rev.*, 91, 113–154.

Pollock, C. J., et al. (2001), First Medium-Energy Neutral Atom (MENA) images of Earth's magnetosphere during substorm and storm-time, *Geophys. Res. Lett.*, 28(6), 1147–1150.

Pollock, C. J., et al. (2003), The role and contributions of energetic neutral atom (ENA) imaging in magnetospheric substorm research, *Space Sci. Rev.*, *109*, 155–182.

Pollock, C. J., A. Isaksson, J.-M. Jahn, F. Sorass, and M. Sorbo (2009), Remote global-scale observations of intense low-altitude ENA emissions during the Halloween geomagnetic storm of 2003, *Geophys. Res. Lett.*, *36*, L19101, doi:10.1029/2009GL038853.

Reeves, G. D., et al. (2003), IMAGE, POLAR, and geosynchronous observations of substorm and ring current ion injection, in *Disturbances in Geospace: The Storm-Substorm Relationship*, *Geophys. Monogr. Ser.*, vol. 142, edited by A. S. Sharma, Y. Kamide, and G. S. Lakhina, pp. 91–101, AGU, Washington, D. C.

Ritzau, S. M., and R. A. Baragiola (1998), Electron emission from carbon foils induced by keV ions, *Phys. Rev. B.*, *58*(5), 2529–2538.

Roelof, E. C. (1987), Energetic neutral atom imaging of a storm-time ring current, *Geophys. Res. Lett.*, *14*(6), 652–655.

Roelof, E. C. (1997), ENA emissions from nearly mirroring magnetospheric ions interacting with the exobase, *Adv. Space Res.*, *20*(3), 361–366.

Roelof, E. C. (2005), Pressure-driven currents derived from global ENA images by IMAGE/HENA, in *Inner Magnetosphere Interactions: New Perspectives from Imaging*, *Geophys. Monogr. Ser.*, vol. 159, edited by J. L. Burch, M. Schulz, and H. Spence, pp. 153–157, AGU, Washington, D. C.

Roelof, E. C., P. C:son Brandt, and D. G. Mitchell (2004), Derivation of currents and diamagnetic effects from global plasma pressure distributions obtained by IMAGE/HENA, *Adv. Space Res.*, *33*(5), 747–751.

Skoug, R. M., et al. (2003), Tail-dominated storm main phase: 31 March 2001, *J. Geophys. Res.*, *108*(A6), 1259, doi:10.1029/2002JA009705.

Smith, C. W., J. L'Heureux, N. F. Ness, M. H. Acuna, L. F. Burlaga, and J. Scheifele (1998), The ACE magnetic fields experiment, *Space Sci. Rev.*, *86*, 613–632.

Stone, E. C., A. M. Frandsen, R. A. Mewaldt, E. R. Christian, D. Margolies, J. F. Ormes, and F. Snow (1998), The advanced composition explorer, *Space Sci. Rev.*, *86*, 1–22.

Vallat, C., et al. (2004), First comparison between ring current measurements by Cluster/CIS and IMAGE/HENA, *J. Geophys. Res.*, *109*, A04213, doi:10.1029/2003JA010224.

Williams, D. J., E. Keppler, T. A. Fritz, and B. Wilken (1978), The ISEE 1 and 2 medium-energy particles experiment, *IEEE Trans. Geosci. Electron.*, *16*(3), 270–280.

Zaniewski, A. M., X. Sun, A. Gripper, E. E. Scime, J.-M. Jahn, and C. J. Pollock (2006), Evolution of remotely measuredinner magnetospheric ion temperatures during a geomagnetic storm, *J. Geophys. Res.*, *111*, A10221, doi:10.1029/2006JA011769.

P. C. Brandt and E. Roelof, Johns Hopkins University Applied Physics Laboratory, Laurel, MD 20723, USA.

N. Buzulukova and M.-C. Fok, NASA Goddard Space Flight Center, Greenbelt, MD 20771, USA.

J. Goldstein, D. J. McComas, and P. Valek, Southwest Research Institute, San Antonio, TX 78228, USA.

J. D. Perez, Department of Physics, Auburn University, Auburn, AL 36849, USA.

R. Skoug, Los Alamos Laboratory, Los Alamos, NM 87545, USA.